New constraints from seismology and geodesy on the Mw = 6.4 2008 Movri (Greece) earthquake: evidence for a growing strike-slip fault system,

Anna Serpetsidaki, P. Elias, M. Llieva, Pascal Bernard, Pierre Briole, Anne Deschamps, Sophie Lambotte, H. Lyon-Caen, E. Sokos, G.-A. Tselentis

Geophysical Journal International

Geophys. J. Int. (2014) **198,** 1373–1386 doi: 10.1093/gji/ggu212
GJI Seismology

New constraints from seismology and geodesy on the $M_w = 6.4$ 2008 Movri (Greece) earthquake: evidence for a growing strike-slip fault system

A. Serpetsidaki,[1] P. Elias,[2,3] M. Ilieva,[2,4] P. Bernard,[5] P. Briole,[2] A. Deschamps,[6] S. Lambotte,[2,7] H. Lyon-Caen,[2] E. Sokos[1] and G.-A. Tselentis[1]

[1]*Seismological Laboratory, University of Patras, GR-26504 Patras, Greece. E-mail: annaserp@upatras.gr*
[2]*Laboratoire de Géologie, Ecole Normale Supérieure, CNRS, F-75005 Paris, France*
[3]*National Observatory of Athens, GR-15236 Athens, Greece*
[4]*Bulgarian Academy of Sciences, Sofia 1113, Bulgaria*
[5]*Institut de Physique du Globe de Paris, CNRS, F-75238 Paris, France*
[6]*GéoAzur, Université de Nice Sophia Antipolis - CNRS - IRD - OCA, GéoAzur, F-06560 Valbonne, France*
[7]*Now at Ecole et Observatoire des Sciences de la Terre, CNRS, F-67084 Strasbourg, France*

Accepted 2014 June 2. Received 2014 June 2; in original form 2014 January 22

SUMMARY

The 2008 $M_w = 6.4$ Movri earthquake ruptured a NNE right lateral strike-slip fault about 30 km south of the city of Patras. Although some strike-slip activity on minor faults was known, there was no tectonic evidence of large scale NS striking fault and such a large event was not anticipated. Following the event, a network of six stations was installed for 4 months in the epicentral area in order to monitor aftershocks and in particular the northern part of the rupture area closest to the city of Patras. We combine these new aftershock observations with GPS measurements of an already existing geodetic network in the area performed just after the earthquake, as well as with SAR interferograms, together with already published source studies, in order to refine already proposed models of this event. The combined data set allows defining much more accurately the lateral and vertical limits of the rupture. Its length inferred from geodesy is ∼15 km and its modelled upper edge ∼17 km. The seismic moment then constrains the lower edge to coincide, within a few kilometres, with the Moho interface. The absence of seismicity in the shallow crust above the co-seismic fault is interpreted as a result of the decoupling effect of possible presence of salt layers above the rupture area, near 14 to 16 km in depth, which favours our interpretation of an immature strike-slip fault system, compatible with the absence of surface ruptures. The immature character of this large crustal fault is further suggested by the high variability of focal mechanisms and of fault geometries deduced from aftershock clusters, in the strike direction. Its geometry and mechanism is consistent with the crustal shear, striking NNE, revealed by GPS in this region. This shear and faulting activity might be generated by the differential slip rate on the subduction interface, 50 km to the south, leading to a north-northeastward propagating strike-slip fault zone. The wide extension of the aftershock distribution forming a NNE alignment, beyond the rupture area towards the north, suggests a localization process of the shear strain, which could be the preliminary stage of fault propagation further to the NNE. An alternative speculative model for this regional stress could be the existence of a well-developed NNE striking shear zone within the uppermost mantle, marking at depth the southward propagation of the northern branch of the North Anatolian fault. Both models may not be exclusive of each other, and in fact their sources may be mechanically interdependent.

Key words: Satellite geodesy; Radar interferometry; Earthquake dynamics; Seismicity and tectonics; Dynamics and mechanics of faulting.

1 INTRODUCTION

On 2008 June 8 (12:25 UTC) a $M_w = 6.4$ earthquake occurred near Movri mountain, in northwest Peloponnesus, 30 km south of the city of Patras and was felt throughout mainland Greece. Although strong earthquakes are common in western Greece, this event took place in a region free of strong events throughout the historic observation period (Gallovic *et al.* 2009; Papadopoulos *et al.* 2010).

The area lies in the northern part of the Western Hellenic arc where the African Plate subducts under the Aegean, about 100 km southeast of the Cephalonia transform fault that accommodates the transition between subduction of the Ionian oceanic slab in the south and subduction/collision of the more buoyant Adriatic continental slab in the north (e.g. Royden & Papanikolaou 2011). The earthquake is located in a transition zone: to the NE, the highly seismogenic and rapidly deforming areas of the Patras Gulf and the Corinth Rift are dominated by north–south extension while to the southwest, the Ionian Sea seismicity is mainly related to the active subduction. Internal deformation based on historical triangulation or global positioning system (GPS) measurements (Charara 2010; Briole *et al.* 2013; Stiros *et al.* 2013) is small and poorly resolved but indicates NE–SW shear. Only a few reliable fault plane solutions for the area were available before the 2008 earthquake, due to the low level of seismic activity, indicating extensive strike-slip motion and favouring dextral strike-slip motion parallel to the strike of the Cephalonia strike-slip fault. (Kiratzi & Louvari 2003; Vernant *et al.* 2014). This strike also coincides with that expected for a hypothetic westward continuation of the North Anatolian fault (NAF).

The moment tensor (MT) solution together with early aftershock locations of the 2008 event (e.g. Gallovic *et al.* 2009) indicate NNE right lateral strike-slip faulting not related to any major fault mapped in the area. Although the earthquake caused damage and triggered secondary phenomena like rock-falls and landslides, no surface rupture directly related to fault slip was observed (Ganas *et al.* 2009; Margaris *et al.* 2010). Koukouvelas *et al.* (2009) studying the surface deformation, concluded that the Movri earthquake is related to a high angle blind fault. Gallovic *et al.* (2009) based on a regional waveform inversion and a line source model revealed predominantly unilateral rupture propagation and at least two main slip patches, while the largest slip coincides with the region of the least abundant aftershocks. Konstantinou *et al.* (2009) from a similar set of data also concluded that the earthquake consisted of a high amplitude slip patch located at depth between 8 and 15 km, and of smaller patches in the deeper parts of the fault down to 30 km depth. On the other hand, Papadopoulos *et al.* (2010) based on National Observatory of Athens aftershock locations and macroseismic observations suggested that the earthquake ruptured an area about 40 km long between 5 and 20 km depth implying up to 8 cm of vertical displacement to the northwest of the epicentre. However, based on one synthetic aperture radar (SAR) interferogram Feng *et al.* (2010) concluded that the earthquake did not produced any observable deformation, whereas the analysis of the permanent GPS RLS station located ∼10 km west of the rupture plane (Ganas *et al.* 2009) shows a co-seismic offset to the north of ∼7 mm consistent with the right-lateral kinematics of the source.

In this study, we present new seismological data from a dense mobile network installed in the epicentral area on 2008 June 14 for a period of 4 months (Fig. 1), as well as a new GPS and SAR-based deformation field. The results from both seismology and geodesy are jointly used to better constrain the depth and lateral extent of the rupture and to propose an updated faulting model for the Movri earthquake. Finally, we discuss the implications for the seismotectonics of the area and the relationship of this earthquake with neighbouring plate boundaries.

2 CONSTRAINTS FROM SEISMICITY

2.1 Location–relocation

The main shock and aftershocks were recorded by the Hellenic Unified Seismological Network (HUSN). The events spanning the first month following the main shock were manually located by University of Patras Seismological Laboratory using the Atlas Nanometrics software. In addition, seven mobile seismological stations from the French national SISMOB network were installed 6 d after the main shock for almost 4 months. The network was installed to precisely monitor the aftershocks as only one permanent station (RLS) from HUSN is located within 20 km of the epicentral area. The implementation focussed on the northern termination of the main fault closest to Patras city but the network geometry combined with HUSN stations (Fig. 1) allowed most aftershocks to be well recorded.

Stations consisted of broad-band three-component seismometres (GURALP-CMG40) and high-dynamic recorders at 100 Hz (four TAURUS – Nanometrics and three OSIRIS – Agecodagis) equipped with continuous GPS timing. The interstation spacing was about 10 km. We used the software SeisGram2K (Lomax 1999) for manual pick of the *P* and *S* phases. According to selection criteria (high signal to noise ratio and at least four stations with *P* and *S* picks), 1108 events were selected. The distribution of these stations and the period of their operation provide detailed data which complement the initial picture of the rupture zone given by the early period aftershocks located from HUSN data (Fig. 2).

The HYPOINVERSE software (Klein 2002) was used for hypocentre determination. The data from 13 HUSN stations and 6 SISMOB stations were jointly used for the initial location with the Tselentis *et al.* (1996) 1-D crustal model (Table 1), while the V_p/V_s ratio was set to 1.78.

The sequence was then relocated using HYPODD (double difference) software (Waldhauser 2001). HYPODD determines relative locations within clusters, using the double difference algorithm, developed by Waldhauser & Ellsworth (2000). It improves relative location accuracy by strongly reducing the influence of the velocity structure on locations.

Catalogue *P*- and *S*-wave arrival times (63 752 phases) deriving from stations within 50 km from the epicentral area were used. 968 initial locations including data from 10 stations (Fig. 2) were combined in the procedure, and parameters were set, following Waldhauser's (2001) suggestions for data sets containing a number of events smaller than 1000. The double-difference residuals for the pairs of earthquakes at each station were minimized by weighted least squares, using the method of conjugate gradient least squares. The velocity model used in the relocation was the model used in the initial location process. 872 events were relocated and clustered in the area of interest. The HYPODD final result has a mean root mean square (rms) of 0.02 s and mean location and *t* formal uncertainty smaller than 10 m and 10 ms, respectively. The relocated events are more densely distributed, compared to the initially located ones. As the early aftershocks (first 7 d after the main shock, in black on Fig. 3), the HYPODD relocated aftershocks follow, more or less, the NNE–SSW direction of the main shock fault, while their surface and depth distribution indicates a separation into smaller clusters, which are described and discussed below (Fig. 3).

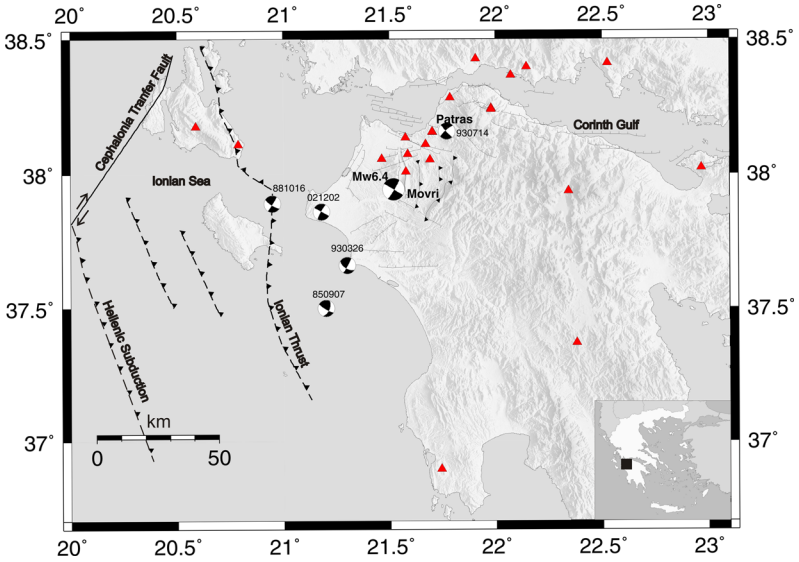

Figure 1. Seismological stations (red triangles) used to analyse the Movri earthquake. Faults are mapped in the study area after Feng *et al.* (2010), Sokos *et al.* (2012) and CRL (http://crlab.eu). Moment tensor solutions from recent strike-slip earthquakes are also plotted (850907, 881016, 930326, 930714 after Kiratzi & Louvari 2003, 021202 after Serpetsidaki *et al.* 2010).

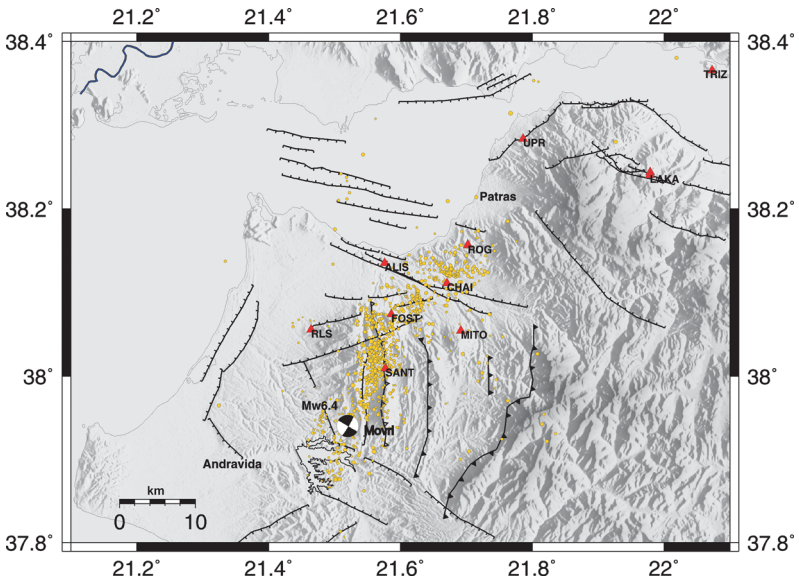

Figure 2. Aftershocks distribution in the study area located using HYPOINVERSE software.

Table 1. 1-D crustal model.

$V_p/V_s = 1.78$	
V_p (km s^{-1})	Depth (km)
5.70	0.00
6.00	5.00
6.40	18.00
7.90	39.00

2.2 Clustering of the seismicity

The spatial distribution of the relocated aftershocks is rather complex and in order to discuss and interpret it, the aftershocks were classified in seven clusters according to HYPODD relocation results (Fig. 4). At depth the seismicity is distributed in two zones: a shallow one between 5 and 14 km and a deeper one between 16 and 26 km. The upper 5 km and a layer between 14 and 16 km are free of seismic events (Fig. 4b). We identified three different clusters within the shallow seismic zone and four clusters within the deeper one (Fig. 4). The clusters are distinctly coloured in order to facilitate their relative 3-D positions, in case of overlapping in the selected projections.

The largest cluster is the yellow one, elongated in the NNE–SSW direction and confined at depth between 16 and 26.5 km. It includes all deep earthquakes of the southern part of the aftershock zone and is limited to the north by earthquakes forming a WSW–ENE elongated structure (magenta cluster) and separated from it by a gap of 1–2 km. Most of the events of this cluster form a 4–5 km wide structure aligned with the main fault strike as defined from MT solution. This cluster includes the main shock hypocentre and defines a vertical zone 18 km long and 10 km wide. We interpret it as representing the main rupture area. This interpretation is supported by the analysis of the co-seismic deformation field discussed in Section 3. The fact that aftershocks in the vicinity of the main

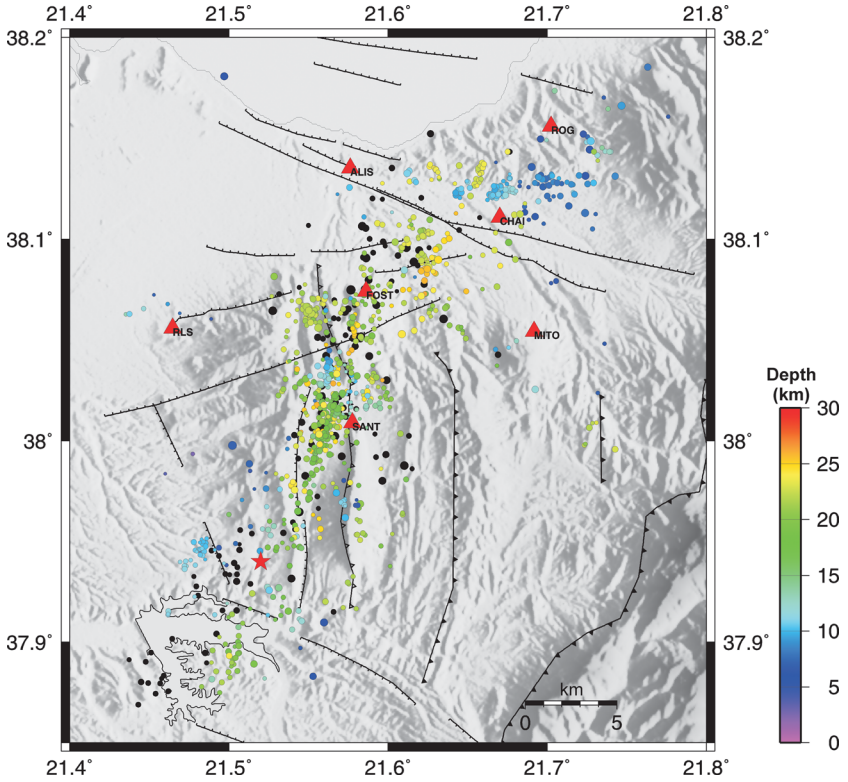

Figure 3. HYPODD relocated aftershocks with colours as a function of depth. Red star indicates main shock epicentre and black dots are the relocated aftershocks occurring the first week (after Gallovic *et al.* 2009).

shock hypocentre are few suggests that most of the stored energy was released by the main shock.

The cyan cluster includes all shallow events of the southern part of the aftershock zone. Its eastern part does not exhibit any peculiar structure but the western part, that was mainly activated between July 1 and 15, forms a dense pattern located off the main fault strike which seems to be dipping SSE (Fig. 4d). The cluster covers an area 10 km × 7 km with depths of events ranging from 7 to 14 km.

On top of the northern part of the yellow cluster, the black cluster (Fig. 4a) forms a NNW–SSE elongated cluster steeply dipping to the SW. This cluster has a completely different structure than the yellow one and cannot be considered as an upwards continuation of it. The events align on a well defined, almost planar structure 5 km long and 6 km wide extending at depths between 8 and 14 km. The strike and dip of this structure does not coincide with any already mapped fault. Moreover, it is not connected to the magenta cluster since they are dipping in different directions and angles (Fig. 4).

North of the yellow cluster, we identified three different deep clusters (magenta, blue and green), each characterized by a different internal structure. The events of the magenta cluster form an ENE–WSW, 9-km-long striking structure (Fig. 4a). At depth the structure extends between 17 and 26 km and is almost vertical (Figs 4b and d). It differs from the blue cluster lying just NNE both in direction and dip. The blue cluster extends from 19 to 26 km depth and is about 5 km long. It is not connecting to the green cluster since they differ in direction and dip angle. The green cluster in map projection (Fig. 4a) appears divided in two separate structures but at depth (Fig. 4d) it forms a unique structure, which dips to the North. The structure has E–W direction, 5 km length and 4 km width. It is not connected to the red cluster's events since it is much deeper, between 20 and 24 km and it is dipping to the opposite direction.

At the northern end of the aftershocks area, the red cluster includes shallow events between 5 and 14 km. This cluster, mainly activated after July 15, contains two dense groups of events and forms a structure 6.5 km long and 9 km wide. The whole structure is striking W–E to WNW–ESE, and both groups are dipping to NNE (Figs 4b and c). The upward prolongations of both clusters meet the surface close to the mapped structure (F), which is a large WNW–ESE striking normal fault.

Among the three shallow clusters, only the northernmost red one can clearly be associated with a known fault, a normal fault orthogonal to the mean strike of the Movri rupture. The black cluster defines very well, at depth, a fault plane activated by the Movri earthquake, while the blue cluster to the south does not exhibit a very clear structure. In the three cases, these shallow structures are decoupled from the deeper clusters. The three deep northern clusters (magenta, blue and green) are clearly distinct from the southern (yellow) one.

2.3 Focal mechanism-MT

The fault plane solutions were determined using the FPFIT program (Reasenberg & Oppenheimer 1985) with the events' azimuths and angles of incidence computed from the double difference relocation. The main criteria to characterize the quality of the final solution are the norm misfit function F_j ($F_j = 0.0$ represents a perfect fit) and the station distribution ratio ($0.0 \leq \mathrm{STDR} \leq 1.0$). The uncertainties (errors) in strike, dip and rake, ΔSTR, ΔDIP, ΔRAK of the final solutions should be smaller than 20° (Reasenberg & Oppenheimer 1985).

Out of the 968 events, we selected those with nine or more *P*-wave first arrivals as input to FPFIT. Only events leading to a

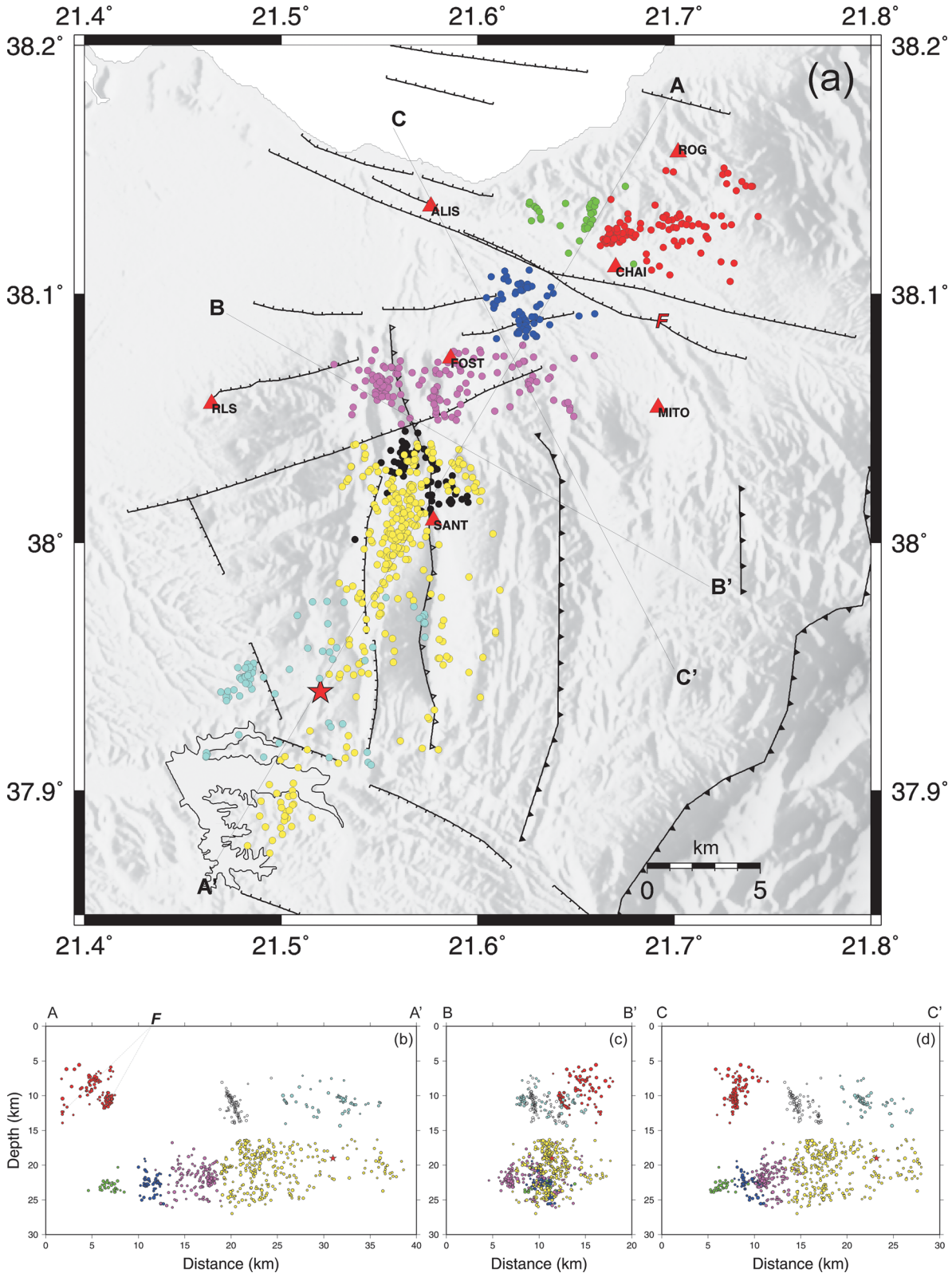

Figure 4. (a) Relocated aftershocks classified in clusters. Each cluster is identified by its colour (b) cross section AA′ parallel to the strike of the fault (c) cross section BB′ perpendicular to the strike (d) cross section CC′ at 45° from the strike. Location of cross-sections are indicated in (a) dashed lines and in (b) indicates possible upward prolongation of the red cluster outcropping at point F indicated in (a). Red star indicates relocated hypocentre of the main shock (Gallovic *et al.* 2009).

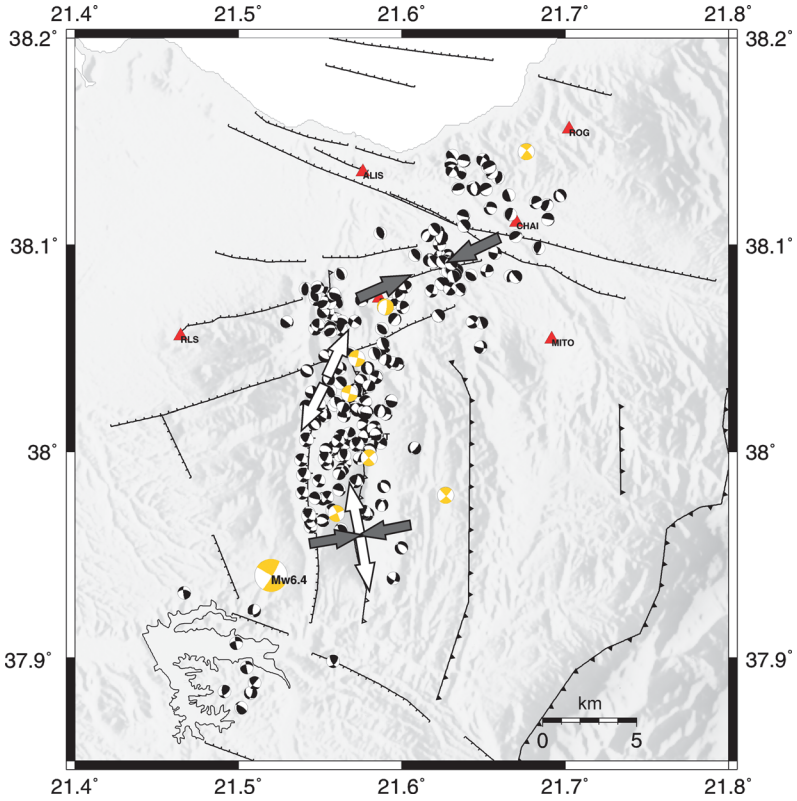

Figure 5. Moment tensor of the main shock and major aftershocks (orange beach-balls) and aftershocks focal mechanisms (black beach-balls). The principal compression axis S1 (black arrow) and principal tension axis S3 (white arrow) according to stress tensor inversion results are also plotted.

unique fault plane solution were kept, resulting in a data set of 200 reliable fault plane solutions and well-constrained nodal planes, with mean misfit function F_j, equal to 0.12, mean STDR equal to 0.7 and uncertainties in strike, dip and rake (ΔSTR, ΔDIP, ΔRAK) smaller than 10° (Fig. 5).

In addition a MT determination was performed for the main shock and the major aftershocks using the crustal model of Table 1 and waveforms filtered in the frequency range 0.04–0.1 Hz (Fig. 5, orange beach-balls). The MT inversion was performed by the so-called iterative deconvolution method of Kikuchi & Kanamori (1991), modified for regional distances and encoded by Zahradník *et al.* (2005). Complete waveforms were used without separation of individual phases and full-wave Green functions were calculated by the discrete wavenumber method in a 1-D velocity model. Easy processing is possible due to a user-friendly Fortran-Matlab program package ISOLA (Sokos & Zahradnik 2007). Since the present study involves weak events we used a single point-source model and assumed no volume change. The results are expressed in terms of the double-couple component of the deviatoric solution, represented by the scalar moment, strike, dip and rake of one of the conjugate planes. The variance reduction, which quantifies the observed/synthetic waveforms fit for a MT solution, is considered to indicate a good fit when it is larger than 40 per cent.

The focal mechanisms distributed in the whole study area seem to be dissimilar, which, according to Bowman *et al.* (2003) could be an indication of very low friction on the strike-slip fault, leading easily to a stress field that favours reverse or normal faulting. The focal mechanisms located in the area of the main shock and the southern part of the sequence; corresponding to the yellow cluster, show mainly strike-slip faulting following the pattern of the main shock. Many focal mechanisms located in the central part of the sequence within the black cluster (Fig. 4) indicate normal faulting (Fig. 5). This suggests the existence of a minor normal fault striking WNW–ESE. The dip angle estimated by the seismicity distribution (~70°) is consistent with the mean dip calculated from the normal focal mechanisms solutions of the cluster (67°). To the north many focal mechanisms indicating thrust faulting on more or less NW–SE striking planes are part of the blue and magenta (Fig. 4) clusters, suggesting a local change in the stress regime. Kamberis *et al.* (2000) using aerial photographs, field observations and onshore seismic profiles also revealed the co-existence of strike-slip faulting with thrust and normal faults in the study area, striking NW and WNW, respectively.

The MT solutions of the largest aftershocks mainly located in the southern part of the aftershock area indicate strike-slip faulting as the main shock. One notable exception is the MT of one aftershock located in the area of shallower focal mechanisms, which also indicate normal faulting. In the NNE, due to quality limitations, only a few focal mechanisms were calculated, which does not allow trustworthy conclusion. The case of an aftershock sequence produced by a buried strike-slip fault, whose propagation to the surface is resisted by a zone of mixed-mode faulting (Bowman *et al.* 2003), may apply in the study area.

2.4 Stress tensor inversion

The focal mechanisms and MT solutions were used to invert the stress tensor and reveal the main stress regime in the area. The stress inversion was carried out using the Zmap software (Wiemer & Zuniga 1994), in order to calculate the directions of the principal stress axes S_1, S_2, S_3 and the shape factor R ($R = (S_2 - S_1)/(S_3 - S_1)$), which indicates the magnitude of S_2 relative to S_1 and S_3.

Table 2. Stress Tensor inversion results.

Area	Fault type	S1 Trend/plunge	S2 Trend/plunge	S3 Trend/plunge	R	β	Number of mechanisms
Southern part 15 km < depth < 30 km (yellow cluster)	Strike-slip	−100/28	84/61	−10/2	0.3	30	73
Northern part 15 km < depth < 30 km (blue, magenta clusters)	Thrust	−115/11	152/14	11/72	0.7	38	32, 58
Central part 0 < depth < 15 km (black cluster)	Normal	−129/40	128/15	22/45	0.18	39	25

The misfit angles between observed and theoretical slip directions are important in evaluating the reliability of the solution of a stress tensor inversion. For fault plane solution errors varying from 10 to 25 degrees, the misfit angle (β) can range from 30° to 45° (Michael 1991), indicating that stress inversion results with misfits lower or in this range are considered acceptable and that the stress field is approximately homogeneous. Michael's method was applied; according to Michael (1987) in order to increase the reliability of the solution, it is important to test the effects of subsets (clusters) of the data on the final solution. Thus, numerous inversions were run with varying subsets (e.g. magenta and blue clusters together and individually) of the whole data set to evaluate whether the stress field in any two neighbouring regions is significantly different. On this basis, we decided to split the area in three subsets. The results are summarized in Table 2 and plotted in Fig. 5. The southern part, which in Fig. 4 appears in yellow and represents the main shock area, is characterized by strike-slip faulting and the direction of the major compression axis is NNE–SSW. To the northern limits of this area but at shallower depth, where the structure of a minor fault (black cluster, Fig. 4) exists, the faulting type is normal. In this shallower area the major compression axis has a NE–SW horizontal component, and the horizontal component of tension is NNE–SSW. The horizontal tension direction is consistent with the distribution of epicentres (Fig. 4, in black) in the area, which suggests a fault plane striking NNW–SSE. The stress tensor inversion of the aftershocks located to the north, in the magenta and blue clusters, indicates a thrust faulting environment with a compression direction oriented NE–SW (Fig. 5). The analysis of the focal mechanisms inside the green and red clusters indicates normal faulting but, since only few focal mechanisms were available for the inversion process, we consider this result uncertain and do not interpret it.

3 CONSTRAINTS FROM GPS AND SAR INTERFEROMETRY ON FAULTING MODEL

3.1 GPS data

We used data from eighteen GPS sites belonging to permanent networks (Corinth Rift Lab – CRL, National Observatory of Athens – NOA, Eidgenössische Technische Hochschule Zürich – ETHZ, Hellenic Positioning System – HEPOS) and campaign networks (eight CRL campaign points). Fig. 6 shows the location of the GPS sites and the co-seismic vectors. The data from CRL and NOA were processed using the GIPSY (v 6.1.2) software.

At RLS0, the only permanent station close to the epicentre, the co-seismic offset is very clear in the time-series (fig. 9 of Ganas *et al.*

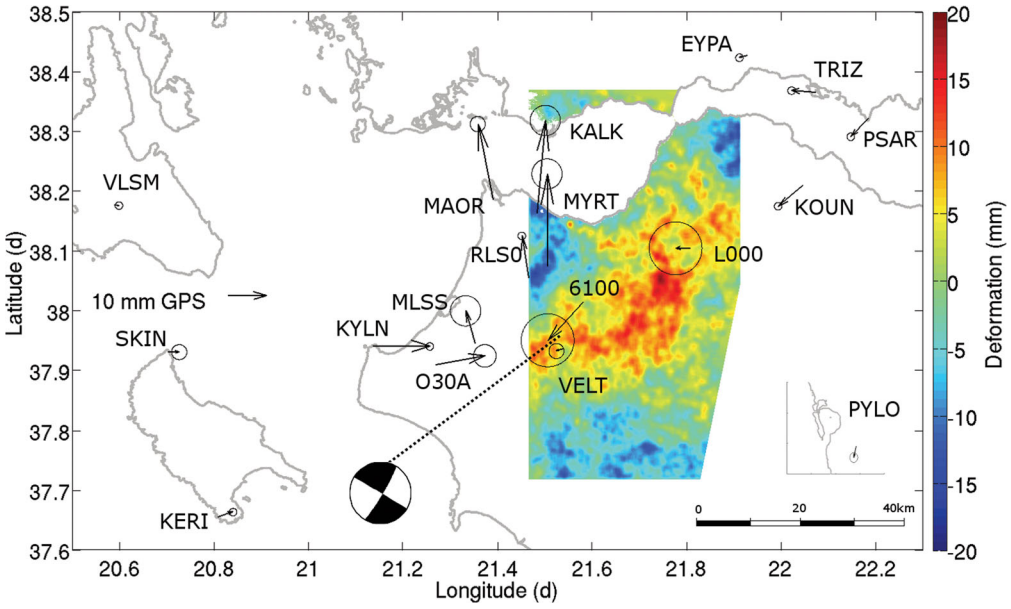

Figure 6. Horizontal co-seismic GPS vectors and averaged and filtered SAR interferogram (from nineteen co-seismic interferograms). Positive values indicate a displacement away from the satellite in the line of sight. The inset shows the vector at the PYLO station, located south of the main map.

Table 3. Horizontal co-seismic displacements and uncertainties at eighteen GPS sites.

Name	Network	Long. (°)	Lat. (°)	δ_E (Mm)	δ_N (mm)	σE (Mm)	σN (mm)	M_E (mm)	M_N (mm)
6100	CRL	21.5796	38.0138	− 9.2	− 7.9	7.0	7.0	− 2.7	0.0
KALK	CRL	21.4831	38.1641	2.2	19.3	4.0	4.0	− 3.4	13.6
KYLN	CRL	21.1364	37.9406	15.0	0.0	1.0	1.0	10.2	1.8
L000	CRL	21.8079	38.1047	− 3.9	0.0	4.0	4.0	− 11.2	− 6.3
MAOR	CRL	21.3897	38.1862	− 4.0	15.8	2.0	2.0	− 5.5	13.4
MLSS	CRL	21.3520	37.9456	− 2.5	6.8	4.0	4.0	7.9	2.8
MYRT	CRL	21.5043	38.0747	0.0	19.3	4.0	4.0	− 2.6	10.0
VELT	CRL	21.5396	37.9368	− 1.9	− 0.5	7.0	7.0	− 0.5	− 0.7
EYPA	CRL-p	21.9285	38.4268	− 2.1	− 0.4	4.0	4.0	− 2.2	− 0.8
KOUN	CRL-p	22.0459	38.2095	− 6.5	− 4.3	1.0	1.0	− 6.9	− 3.6
PSAR	CRL-p	22.1843	38.3218	− 4.6	− 3.8	1.0	1.0	− 4.2	− 2.3
PYLO	CRL-p	21.7420	36.8956	− 0.6	− 2.3	1.0	1.0	0.6	− 2.1
TRIZ	CRL-p	22.0727	38.3654	− 6.3	0.4	1.0	1.0	− 3.6	− 2.1
KERI	ETHZ-p	20.8080	37.6551	4.0	1.0	1.0	1.0	5.2	2.2
SKIN	ETHZ-p	20.7020	37.9310	3.0	0.0	2.0	1.0	4.2	0.8
030A	HEPOS	21.2687	37.9088	13.0	2.0	3.0	3.0	13.1	3.4
RLS0	NOA-p	21.4648	38.0559	− 1.7	8.7	1.0	1.0	− 3.4	9.9
VLSM	NOA-p	20.5887	38.1768	1.2	− 0.1	1.0	1.0	1.2	0.6

2009), and it is the only site where a vertical offset is observed. After correcting the co-seismic offset, the coordinate time-series of RLS0 show no post-seismic deformation. We could not see either post-seismic deformation at our campaign stations VELT and MLSS installed on June 9 and operated during three weeks, and Feng *et al.* 2010 report no post-seismic deformation at the nine GPS sites they installed after the earthquake.

In the permanent stations other than RLS0, the co-seismic signal is too small to be clearly visible by calculating the difference between the day before and the day after the earthquake. Its retrieval implied averaging long sets of pre- and post-event coordinates. For that the time-series were beforehand de-trended from the 'long-term' velocity of the site and from an annual tropospheric effect (assumed to be sinusoidal). The difference was then calculated between 1 yr of coordinates before and 1 yr of coordinates after the event, assuming no significant post-seismic signal as established before. We could not process the data from the ETHZ sites KERI and SKIN and from the HEPOS site 030A which were not available, and for those sites we used the offsets published by Muller (2011) and Gianniou (2011).

At the eight campaign points, post-seismic measurements were performed in 2008 June immediately after the earthquake and renewed in 2011 and 2012 September. At the same points, measurements had been performed in 1995, 1998, 1999, 2000, 2003 and 2006. Thanks to the multiple temporal observations and the relatively long time window, the co-seismic offset could be separated from the 'long-term' velocity at those points.

All co-seismic displacements (Table 3), especially those in the near field, are exceptionally small for such a crustal strike-slip earthquake of magnitude M_w 6.4. This crude observation indicates that the fault did not rupture the upper-most part of the crust. In further modelling the amplitude of the GPS displacements will play a major role in constraining the depth at which the rupture stopped. Table 3 contains the horizontal co-seismic displacements and uncertainties at the 18 stations ('p' in network column indicates permanent sites). M_E and M_N columns contain the displacements computed with our final model (see below). More information on the networks and data can be found at http://crlab.eu for CRL data (see also Avallone *et al.* 2004) and at http://www.gein.noa.gr/services/GPS/noa_gps.html for NOA data.

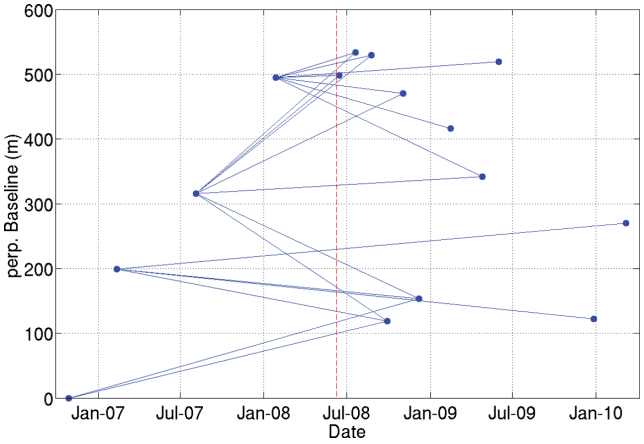

Figure 7. Plot of the dates of the participating ASAR/ENVISAT acquisitions versus the baselines of the interferograms used in the study. The red dashed line indicates the date of the earthquake.

3.2 SAR interferometry data

Fifteen acquisitions of descending I2 mode of the ASAR instrument of the European satellite ENVISAT (Fig. 7) were used to calculate 132 interferograms (4 × 20 multilook) over the epicentral area. Interferograms were calculated using the ROI-PAC software (Rosen *et al.* 2004). The topography effect was corrected by using Ktimatologio S.A. digital elevation model re-projected from transverse Mercator projection of GGCS87 Datum with cell size of 5 m × 5 m to geographic projection of WGS84 datum with cell size 0.0002°N × 0.0002°E.

All interferograms are noisy with limited coherence, due to the vegetated land cover and the steep slopes. They also contain atmospheric effects at the scale of 1–10 km consistent with the spatial scale of the topography and coasts. As previously pointed out by Feng *et al.* (2010), no obvious co-seismic deformation is visible in single co-seismic interferograms. In order to enhance the common mode co-seismic signal, nineteen finest co-seismic interferograms (the lines in Fig. 7) were selected based on visual inspection of the coherence. They were unwrapped using the SNAPHU software (Chen & Zebker 2002). Due to low coherence the possibility of local

unwrapping errors exists and was considered at a later stage. The expected small deformation field (amplitude less than one fringe) prevented us to use the 'assisted' unwrapping technique developed by Elias *et al.* (2006) to analyse the 1999 Athens earthquake.

We excluded from the unwrapped interferograms the offshore pixels, the ones with low coherence, and the areas where the expected absolute modelled deformation was above 10 mm in order to exclude the co-seismic deformation signal from the following bilinear correction. To minimize possible long wavelength orbital residuals and tropospheric effects we proceeded as follows: we partitioned each interferogram in 65 horizontal and 44 vertical zones of 50 pixels and we applied to each interferogram a linear least square fitting to remove any N–S (and then E–W) trend slope of the average values of the horizontal zones. Simultaneously the mean value of each interferogram was set to zero. We applied an average filter of 1 km × 1 km to the average interferogram plotted in Fig. 6 in order to minimize any high-to-medium frequency common mode noise signal.

A regional deformation pattern can be seen in the averaged interferogram. It is not correlated with the topography since in the east and southeast areas the relief is steep and mountainous while, in the area of the observed deformation, the topography is rather low and smooth. We show below that, although subtle, the averaged interferogram is consistent in location and amplitude with the GPS data and therefore we used it as a (loose) constraint in modelling the co-seismic deformation.

3.3 Modelling of the fault as a dislocation in an elastic and homogeneous half-space

Assuming that the earthquake slip can be modelled by a dislocation on a rectangular fault in an homogeneous elastic half-space (Okada 1992) with average shear modulus $\mu = 30$ GPa, a series of inversions of the horizontal co-seismic GPS displacements was performed to retrieve the main characteristics of faulting geometry. The inversion code (Briole *et al.* 1986) uses the least squares approach proposed by (Tarantola & Valette 1982). The inversion cost function is the rms scatter between the observed GPS planar displacements and the modelled ones.

According to the published fault plane solutions (USGS, CMT, NOA, source http://www.emsc-csem.org), the earthquake ruptured a nearly vertical, strike-slip fault. In the following the rake angle has been set to zero implying pure strike-slip faulting and the fault has been fixed at 90°. The mean strike, according to the fault plane solutions, is ranging between 26° and 30°. We performed forward models and inversions with strikes from 25 to 30°: the overall fit is comparable in the scanned range, being slightly better at 25°. This angle is also the most consistent with the overall alignment of the aftershock sequence (southern cluster, in yellow if Fig. 4). In the following we fixed the strike at 25° and assumed a uniform slip over the fault surface.

The fault centre has been initially constrained to fit the published location of the hypocentre. We performed a series of inversions to assess the sensitivity of our GPS vectors to the fault location and estimate a best fitting centre from GPS. The various models converged in a stable manner (within ∼1–2 km) to the average coordinate of 21.524°E/37.937°N, very close to the hypocentre coordinate of the main shock inferred from seismology.

Then we performed a series of inversions aimed to constrain the depth of the upper limit of the fault and its length. The length was scanned in the range 8–28 km and the depth of the upper edge of the fault in the range 6–21 km. For each inversion we locked the two-forth mentioned parameters and left the width (i.e. the depth of the lower edge) and the slip free. As an additional constraint we imposed an *a priori* consistency with the gCMT seismic moment (http://www.globalcmt.org). We used eq. (1) to link the seismic moment and the fault parameters:

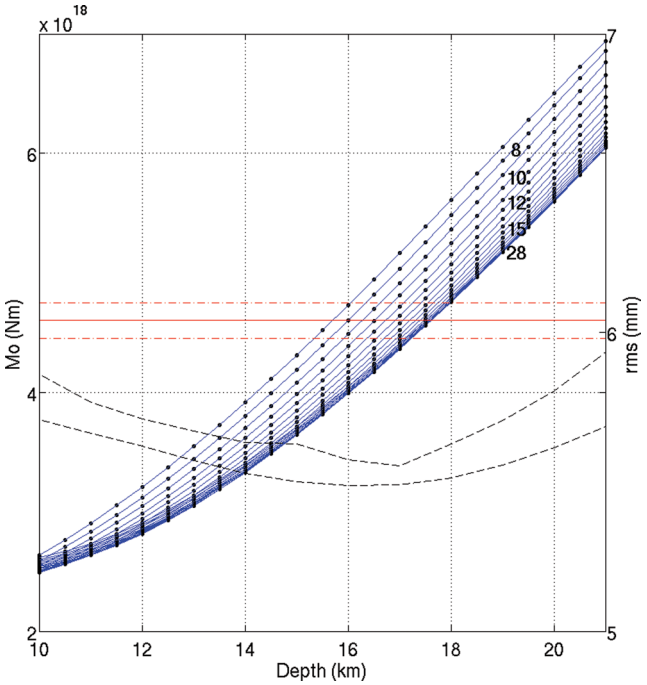

Figure 8. Plot of the depth of the upper limit of the rupture versus M_0 for inversions with centre fault location at 21.524°E/37.937°N. Each blue curve corresponds to a fault length indicated in black on the diagram. On each curve, each point represents the solution of one inversion with the given length (shown in text inside the diagram). The black dashed lines represent the upper and lower limits of the GPS rms scatters for inversions with different lengths fixed. The red line marks the M_0 of gCMT, value and the red dashed line the range of gCMT ± 0.15 10^{18} Nm.

$$M_o = \mu L W D, \tag{1}$$

where $\mu = 30$ GPa shear modulus, L length of the fault, W width of the fault and D slip.

The rms values for all inversions are plotted in Fig. 8. The solutions satisfying the condition $M_0 \sim M_0^{\mathrm{gCMT}} \pm 0.15\ 10^{18}$ N m that is corresponding to a ±3 per cent uncertainty (gCMT, NOA and UOA determinations agree within the 3 per cent range) are taken into account to assess the expected range of fault length and depth. The minimum rms scatter is obtained for the depth of the upper limit of the rupture at 17 ± 1 km (Fig. 8). Fig. 8 shows that, with a M_0 reduced by 35 per cent, the modelled fault would have its upper edge at a depth of 12 km. Thus, our data constrain the upper limit of the fault to be at a depth larger than ∼12 km with a best fit at 17 km and the SAR interferometry, below, will confirm this. Another feature shown by Fig. 8 is the fact that the fault length cannot be well constrained, indeed one can see that all blue lines are concentrated in a narrow tube. This is a consequence of the location of the fault at relative large depth. The GPS points that play the major role in constraining the fault length are those located in the relatively near field, like MAOR, RLS0, 030A, KYLN where the azimuth of the displacement vector is more sensitive to the fault location and length.

Table 4. Acceptable range for the fault parameters and overall best fitting model. The fault was assumed to be vertical with pure strike-slip and its azimuth was not inverted for the calculation of the best fitting model.

Parameter	Acceptable range	Best fitting model
Upper edge centre (East)	21.52 ± 0.03 °	21.52°
Upper edge centre (North)	37.94 ± 0.04 °	37.94°
Depth of upper edge	15.5 ± 3.5 km	17.5 km
Azimuth	27.5 ± 2.5 °	25°
Length	15 ± 3 km	15 km
Width	8.5 ± 1.5 km	8.7 km
Slip	1.2 ± 0.2 m	1.2 m

Our best fit model has the parameters summarized in Table 4. The fit of the GPS vectors is shown in Fig. 9, and the fit of SAR interferogrms in Figs 10 and 11. Our modelled fault corresponds to the location of most of the events of the yellow cluster (Fig. 12).

3.4 Contribution of SAR interferometry to the modelling

Because of the weak and noisy interferometric signal, we have not used SAR interferometry to constrain our model, but we used it to assess its validity and provide additional constraints on the acceptable bounds for some fault parameters. Fig. 10 shows the filtered average interferograms and the modelled deformation field (in the satellite line of sight). Despite the low amplitude of the interferogram and its noise a relatively good fit is obtained between observations and model. Spatially the consistency of the fit can be appreciated in Fig. 10 where the maximum lobe of the model corresponds to the maximum deformation, and the simple visual inspection shows that a translation of a few kilometres of our modelled fault would significantly decrease the fit. Quantitatively, moving the epicentre by 2 and 4 km towards NNE leads to a decreased fit with both the GPS and SAR interferogram data (5.9 and 6.3 mm compared to 5.5 mm best fit).

The good fit of our model to the SAR interferometry can also be evaluated using the cross section shown in Fig. 11. However we notice that SAR interferometry is not helping us to resolve the depth of faulting, for example we show in Fig. 11 that the predicted best-fit displacements (based on the use of the GPS) are not distinguishable with fault depths at 15.5 or 17.5 km. GPS is by far much more efficient to resolve the depth of this faulting. We also noticed that the filtered averaged interferogram is slightly underestimated in comparison with our best-fit model. It seems that this might be due to the fact that, the noise being relatively high, the average filter could have the tendency to decrease the magnitude of the measurements. Another possible explanation could be the fact that in case of biases in the unwrapping of some single interferograms, the expected effect is a decrease of the amplitude of the unwrapped interferogram.

4 DISCUSSION

GPS and SAR interferometry data complement the seismological data to constrain a model with a deep rupture area (yellow cluster) located in the southern part of the entire aftershock area. The inferred, best-fit co-seismic fault is 15 km long, extending at depth from 17 to 27 km with a slip of 1.2 m. In the vicinity of the main shock hypocentre few aftershocks were located, suggesting complete stress relaxation in this area.

Concerning the northern limit of the rupture, the kinematic source inversion by Gallovic *et al.* (2009) suggests a possible continuation of the rupture more than 10 km from the hypocentre to the NNE; the GPS cannot exclude 10 cm of slip to the north since the signal produced at the surface would be undetectable. However, the characteristics of the aftershock seismicity described above show that such a hypothetical NNE prolongation of the main shock strike-slip fault is very unlikely.

Regarding the upward limit of the rupture, the slip model proposed by Konstantinou *et al.* (2009) with the dominant slip patch around 10 km depth north of the epicentre, is not compatible with the surface deformation field as revealed by the GPS and SAR interferometry analysis presented in this study.

The seismicity distribution clearly shows a separation of the main shock rupture area from the shallower clusters. The northern black cluster shows incompatibility with the main cluster direction, while the cyan cluster is lying off the main shock fault area. Thus, the absence of geological evidence for surface rupture together with

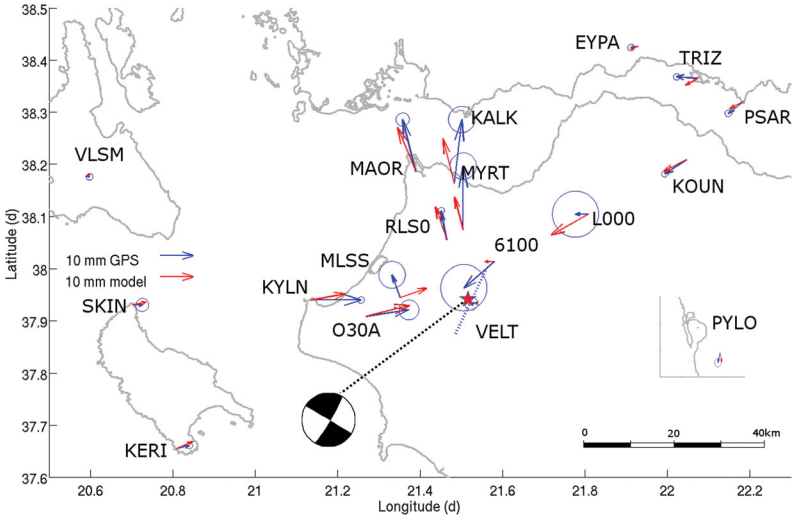

Figure 9. Comparison of observed GPS vectors with calculated ones: in blue the GPS vectors along with their error ellipses and in red the modelled vectors of selected preferred model. Dashed blue line represents the proposed fault location. In the inset, vectors from PYLO located south of the main map, are shown. Red star represents the epicentre.

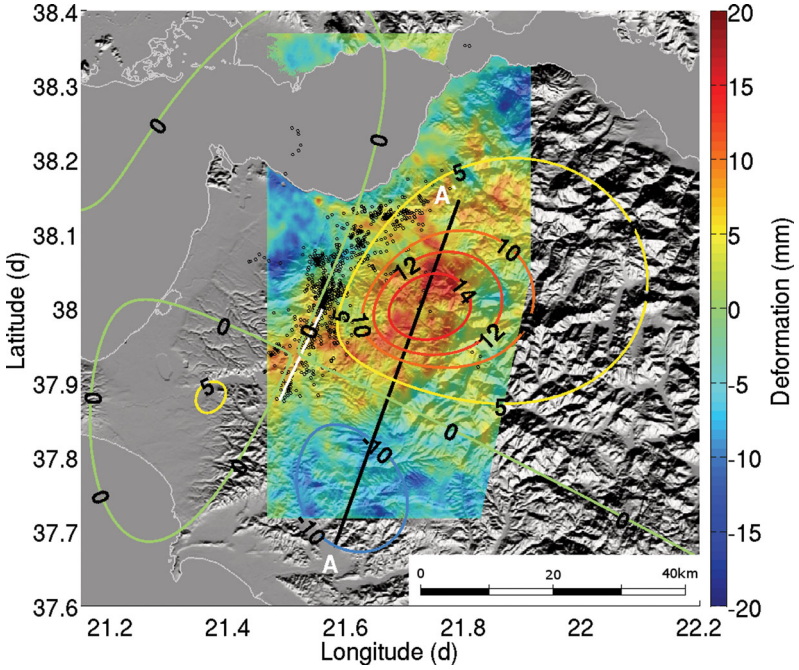

Figure 10. Comparison of SAR interferometry deformation field with that of the preferred model (both in the line of sight, red colour represents deformation towards satellite) discussed in the text. The filtered averaged stacked interferogram is superimposed over shade relief. The modelled deformation field is shown with contour lines. Black circles indicate aftershocks and white line represents the modelled source. The same colour representation is used for the interferogram and the contours. The black line A–A′ corresponds to the trace of the cross section discussed in the text and shown in Fig. 11.

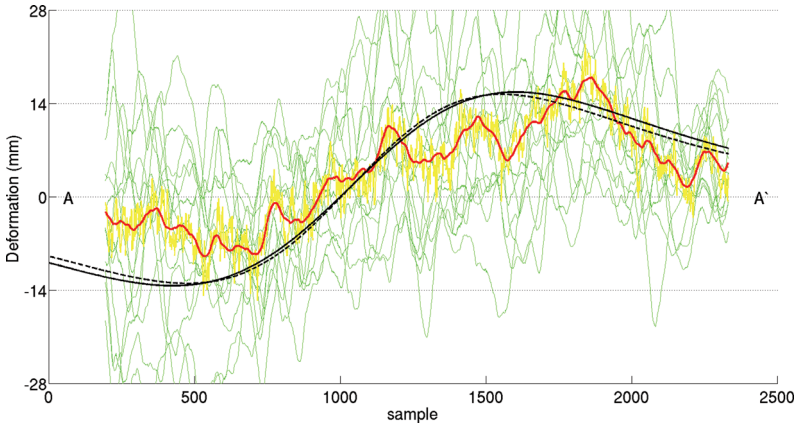

Figure 11. Along cross section A-A4 (see Fig. 10) the line in red shows the ground displacement in the line of sight inferred from the average filtered interferogram. The yellow line is the same quantity but not filtered and the green lines correspond to the single interferograms. The solid black line represents the ground displacement in the line of sight obtained with our model fitting best the GPS data (upper limit of the fault at 17.5 km depth), the dashed line shows the fit when we use a model with the upper limit at 15.5 km depth (corresponding to the lower bound of the blue array at the nominal value of moment tensor in Fig. 8).

the seismicity and GPS results confirm the blind character of the activated strike-slip fault.

The upper boundary of this main fault is characterized to the north by a change in principal stress axis direction, which could prevent the upward propagation of the fault rupture. Also, the aftershock-free region between ∼15 and 16 km in depth may indicate the existence of a layer that blocks the dynamic rupture of the fault. This layer could be composed of the Triassic evaporites which, according to Kamberis *et al.* (2000), are the principal level along which a detachment of the overlying sedimentary succession of thrusts nappes is present.

The bottom limit of the fault is best constrained around 27 km depth from seismological data and the GPS and interferogram modelling. As the depth of the Moho in the area is about 27 km from receiver function analysis (Sodoudi *et al.* 2006), we infer that the Movri earthquake ruptured the lower crust possibly down to the mantle.

To the south, the relative absence of major aftershocks can be explained by the absence of active structures in the lower crust. The southwestern limit of the mantle wedge (dashed blue line in Fig 13a, as determined by Pearce *et al.* 2012) is about 50 km to the SSW of the epicentre, thus too distant to be responsible for limiting the rupture of the main shock. During past years two moderate strike-slip earthquakes (Fig. 1) occurred within the middle to lower crust, in the SSW prolongation of the 2008 main shock, with a similar NNE–SSW strike (see red dots in Figs 13a and b). This suggests

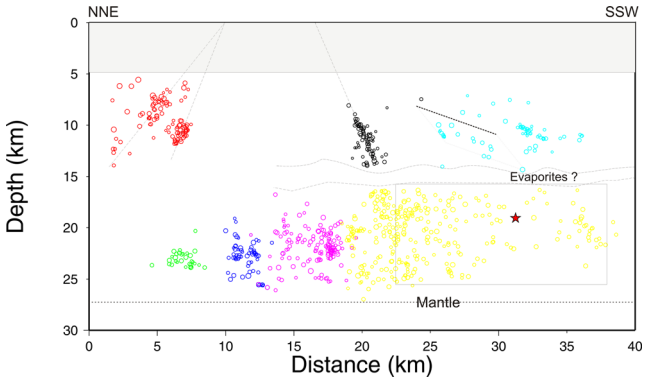

Figure 12. The seismicity projected on the fault plane. The orientation of the *Distance along fault* is from NNE towards SSE. The rectangle represents the most preferred rupture zone for the 2008 Movri earthquake. The seismicity is coloured according to the cluster that each earthquake belongs to.

the existence, or at least the growth, of a large strike-slip structure, connecting the subduction interface to the south to the 2008 rupture area (dotted orange line in Fig. 13a).

All the above suggest that the entire area represents a growing NNE–SSW striking shear zone in relationship with regional interseismic shear strain evidenced by GPS measurements (Charara 2010; Briole *et al.* 2013; Pérouse 2013; Vernant *et al.* 2014) which suggest up to a few mm yr^{-1} of right lateral shear striking NNE-SSW (green arrows in Fig. 13a).

Two main alternative boundary conditions could lead to this shearing process and fault growth. One model would involve the loading from a lithospheric, vertical, major strike-slip shear zone striking NNE–SSW: The southwestern propagation of the NAF, proposed by some authors (Armijo *et al.* 1996; Sachpazi *et al.* 2007; Reilinger *et al.* 2010) could provide such a mechanism (dotted green line in Fig. 13a). However, one would then expect a long-term fault propagation towards the SSW, and hence a decrease in the maturity of the strike-slip zone in the crust from the north to the south. This contradicts with the few available observations which suggest that crustal strike-slip faults do not exist in the few tens of kilometres north to the rupture edge, as evidenced by the highly variable focal mechanisms among the many aftershocks of the 2008 rupture. Whereas the 1985 and the 1993 events in the deeper crust to the south suggest a more possible continuity towards the subduction.

The alternative model involves a differential convergence rate on the interplate subduction contact to the south, with larger values to the SE with respect to the NW (blue dotted ellipses on Fig. 13a). The limit between both contact areas would be in the southward continuation of the 1985–1993–2008 rupture line. This limit is constrained to the west by the interseismic displacement of the Strofades island (GPS station STRO), which has a motion quite similar to Kephalonia. It is further evidenced by the concentration of moderate magnitude thrust interplate events in the NW

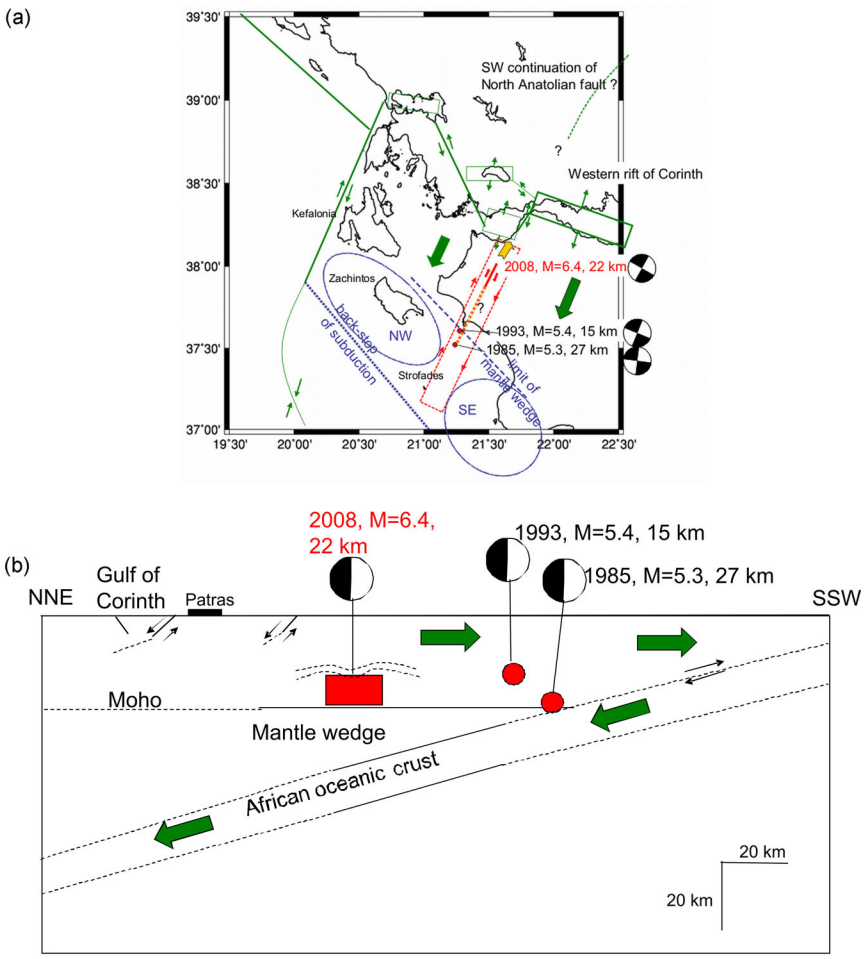

Figure 13. (a) Sketched map of the 2008 event and of its context. (b) Sketched vertical cross-section of the 2008 event and of its context.

zone, whereas the SE region shows more variable focal mechanisms (Kiratzi & Louvari 2003). If due to this lateral variation of interplate slip rate, the growth direction of the NNE–SSW strike-slip fault zone would be from the subduction northward. The 2008 rupture would then mark the present day, northern tip of this localized shear zone. Under this hypothesis, the activation of the region NNE to the 2008 main shock would be part of a preliminary phase of anelastic strain deformation—or damage—, preparing further propagation of the fault to the NNE (yellow arrow in Fig. 13a). We note that the 2008 rupture directivity might have contributed to this focalization of damage, reinforcing its capability of a NNE, along-strike growth.

Both models propose the growth and propagation of a lithospheric strike-slip shear zone. Possibly the best documented example of such a process is the NAF, which propagated westward over about 1500 km, to their western mapped end at the Evia and Corinth rifts, in possibly (at least) 5 Myr (e.g. Hubert-Ferrari *et al.* 2002), hence with mean value of at most 100 km in about 300 kyr.

Considering once more the first model with a southward propagation of the NAF, we note that according to Sachpazi *et al.* (2007), the northern branch of the NAF might be propagating further SSW, confined to the upper mantle and deep crust, reaching the western tip of the rift of Corinth, as suggested by the evidence of a 5 to 10 km high step in the Moho depth. Sachpazi *et al.* (2007) also speculated on its propagation further south, along the eastern edge of the Patras rift, where indeed one has evidence for NNE striking crustal faults with significant strike-slip component. Our results on the 2008 event exclude a southward continuation at crustal depths of such an active shear structure between Patras and the northern limit of the 2008 rupture; but we cannot exclude the southern continuation of a shear structure within the upper mantle.

Considering the second model, with a shear zone growing from the subduction interplate contact, the maximum length of 50 km of the lower crust structure would make this structure quite young: for instance, it would be of the order of 150 kyr, simply taking the same mean propagation velocity as for the NAF.

To summarize, both sources of strain, (1) a hypothetical deep, mantellic southern tip of the NAF, and (2) the differential subduction rate, to the south, may contribute to the shear localization and the fault growth in the deep crust. The available data suggest a more mature lower crust development to the south. Both sources of strain are not mutually exclusive of each other, suggesting the possibility of their coupling through a continuous strike-slip shear zone in the uppermost mantle above the subducting African Plate.

5 CONCLUSION

To conclude, we have shown, through a detailed study of aftershocks combined with GPS and D-Insar studies, that the $M = 6.4$, 2008 Movri earthquake ruptured a deeply rooted, blind, right-lateral strike-slip fault within the lower crust. This fault is possibly connected in the SSW to the subduction interplate, 50 km to the south, through not yet evidenced, blind fault structures and shows no evidence for strike-slip continuation to the NNE. It would be sheared as a result of differential slip rate on the subduction interpolate to the south, with a possible contribution of a deep, lithospheric root of the NA fault to the north.. The 2008 rupture area might thus represent the NNE tip of a large crustal fault growing towards the NNE, which may 1 d be connected to the eastern border of the Patras rift, and merge with the Rio-Patras fault. In the long term, the increase of cumulative displacement on this fault might allow its propagation within the upper crust towards the surface, across the possible 'evaporite' layer. However, for the short term, for what concerns the present day seismic hazard after the 2008 event, major ($M \geq 6$) strike-slip, cascading rupture are unlikely, wether up-dip, or along strike to the NNE, which is of particular importance for assessing the seismic hazard for the city of Patras.

ACKNOWLEDGEMENTS

We acknowledge INSU-CNRS for the SISMOB seismic stations, for the mobile GPS receivers, and for having supported part of the cost of the fieldwork after the earthquake. We acknowledge the European Space Agency for providing us with SAR data from ASAR/ENVISAT (ESA AOE766). We also thank Nicolas Chamot-Rooke for useful discussions on western Greece kinematics. We would like to acknowledge KTIMATOLOGIO S.A. for kindly providing the digital elevation model.

REFERENCES

Armijo, R., Meyer, B., King, G., Rigo, A. & Papanastassiou, D., 1996. Quaternary evolution of the Corinth rift and its implications for late Cenozoic evolution of the Aegean, *Geophys. J. Int.,* **126,** 11–53.

Avallone, A. *et al.*, 2004. Analysis of eleven years of deformation measured by GPS in the Corinth Rift Laboratory area, *C. R. Geosci.,* **336,** 301–311.

Bowman, D., King, G. & Tapponnier, P., 2003. Slip partitioning by elastoplastic propagation of oblique slip at depth, *Science,* **300**(5622), 1121–1123.

Briole, P., De Natale, G., Gaulon, R., Pingue, F. & Scarpa, R., 1986. Inversion of geodetic data and seismicity associated with the Friuli earthquake sequence (1976–1977), *Ann. Geophys.,* **4,** 481–492.

Briole, P. & the CRL team, 2013. Ground deformation across the Corinth rift from 22 years of GPS observations, *EGU General Assembly,* Vienna, Austria, 2013 EGUGA. 1513183B.

Charara, R., 2010. GPS statique, cinématique et haute fréquence appliqué à l'étude de déformations de zones sismiques, *PhD thesis,* University Paris VI.

Chen, C. & Zebker, H., 2002. Phase unwrapping for large SAR interferograms: statistical segmentation and generalized network models, *IEEE Trans. Geosci. Remote Sens.,* **40,** 1709–1719.

Corinth Rift Laboratory. Institute of Geodynamics of the National Observatory of Athens, Available at: www.gein.noa.gr.

Elias, P., Sykioti, O., Kontoes, C., Avallone, A., Van Gorp, S., Briole, P. & Paradissis, D., 2006. A method for rapid elimination of high frequency signal noise and unwrapping artefacts from interferometric calculation, *Int. J. Remote Sens.,* **27**(14), 3079–3086.

European-Mediterranean Seismological Centre. Available at: www.emsc-csem.org.

Feng, L., Newman, A.V., Farmer, G.T., Psimoulis, P. & Stiros, S.C., 2010. Energetic rupture, coseismic and post-seismic response of the 2008 M_w 6.4 Achaia-Elia Earthquake in northwestern Peloponnese, Greece: an indicator of an immature transform fault zone, *Geophys. J. Int.,* **183**(1), 103–110.

Gallovic, F., Zahradnik, J., Krizova, D., Plicka, V., Sokos, E., Serpetsidaki, A. & Tselentis, G-A., 2009. From earthquake centroid to spatial-temporal rupture evolution: M_w 6.3 Movri mountain earthquake, June 8, 2008, Greece, *Geophys. Res. Lett,* **36,** L21310, doi:10.1029/2009GL040283.

Ganas, A., Serpelloni, E., Drakatos, G., Kolligri, M., Adamis, I., Tsimi, Ch. & Batsi, E., 2009. The M_w 6.4 Achaia–Elia (western Greece) earthquake of 8 June 2008: seismological, field, GPS observations, and stress modelling, *J. Earthq. Eng.,* **13,** 1101–1124.

Gianniou, M., 2011. Detecting permanent displacements caused by earthquakes using data from the HEPOS network, in *Proceedings of EUREF 2011 Symposium,* May 25–28 2011, Chisinau, Moldova.

Harvard CMT Catalog. Available at: www.globalcmt.org..

Hubert-Ferrari, A., Armijo, R., King, G., Meyer, B. & Barka, A., 2002. Morphology, displacement, and slip rates along the North Anatolian Fault, Turkey, *J. geohys. Res.,* **107,** doi:10.1029/2001JB000393.

Kamberis, E., Sotiropoulos, S., Aximniotou, O., Tsaila-Monopoli, S. & Ioakim, C., 2000. Late Cenozoic deformation of the Gavrovo and Ionian zones in NW Peloponnesos (Western Greece), *Annali di Geofisica,* **43**(5), 905–919.

Kiratzi, A. & Louvari, E., 2003. Focal mechanisms of shallow earthquakes in the Aegean Sea and the surrounding lands determined by waveform modeling: a new database, *J. Geodyn.,* **36,** 251–274.

Kikuchi, M. & Kanamori, H., 1991. Inversion of complex body waves-III, *Bull. seism. Soc. Am.,* **81,** 2335–2350.

Klein, F.W., 2002. User's guide to HYPOINVERSE-2000, a FORTRAN program to solve earthquake locations and magnitudes, Open-File Rep., U.S. Geol. Surv., 02 171, Version 1.0.

Konstantinou, K.I., Melis, N.S., Lee, S.-J., Evangelidis, C.P. & Boukouras, K., 2009. Rupture process and aftershocks relocation of the 8 June 2008 (M_w 6.4) earthquake in NW Peloponnese, Western Greece, *Bull. seism. Soc. Am.,* **99,** 3374–3389.

Koukouvelas, I.K., Kokkalas, S. & Xypolias, P., 2009. Surface deformation during the M_w 6.4 (June 08, 2008) Movri Mt earthquake in Peloponnese, and its implications for the seismotectonics of Western Greece, *Int. Geol. Rev.,* **52,** 249–268.

Lomax, A., 1999. Java for the seismologist, *ORFEUS Newsletter,* **1**(3).

Margaris, B. *et al.*, 2010. The 8 June 2008 M_w 6.5 Achaia–Elia, Greece earthquake: source characteristics, ground motions, and ground failure, *Earthq. Spectra,* **26,** 399–424.

Michael, A.J., 1987. Use of focal mechanisms to determine stress: a control study, *J. geophys. Res.,* **92,** 357–368.

Michael, A.J., 1991. Spatial variations in stress within the 1987 Whittier Narrows, California, aftershock sequence: new techniques and results, *J. geophys. Res.,* **96,** 6303–6319.

Muller, M.D.M., 2011. Analysis of long-term GPS observations in Greece (1993–2009) and geodynamic implications for the Eastern Mediterranean, *PhD thesis,* ETH, Switcherland.

Okada, Y., 1992. Internal deformation due to shear and tensile faults in a half-space, *Bull. seism. Soc. Am.,* **82,** 1018–1040.

Papadopoulos, G.A., Karastathis, V., Kontoes, C., Charalampakis, M., Fokaefs, A. & Papoutsis, I., 2010. Crustal deformation associated with east Mediterranean strike–slip earthquakes: the 8 June 2008 Movri (NW Peloponnese), Greece, earthquake (M_w 6.4), *Tectonophysics,* **492**(1–4), 201–212.

Pearce, F.D., Rondenay, S., Sachpazi, M., Charalampakis, M. & Royden, L.H., 2012. Seismic investigation of the transition from continental to oceanic subduction along the western Hellenic Subduction Zone, *J. geophys. Res.,* **117,** doi:10.1029/2011JB009023.

Pérouse, E., 2013. Cinématique et tectonique active de l'Ouest de la Grèce dans le cadre géodynamique de la Méditérranée Centrale et Orientale, *PhD thesis,* Université Orsay, Paris Sud.

Reasenberg, P. & Oppenheimer, D., 1985. FPFIT, FPPLOT and FPPAGE: fortran computer programs for calculating and displaying earthquake fault plane solutions, Open-File Rep, U.S. Geol. Surv., OF 95-515.

Reilinger, R., McClusky, S., Paradissis, D., Ergintav, S. & Vernant, P., 2010. Geodetic constraints on the tectonic evolution of the Aegean region and strain accumulation along the Hellenic subduction zone, *Tectonophysics,* **488**(1–4), 22–30.

Rosen, P.A., Henley, S., Peltzer, G. & Simons, M., 2004. Updated repeat orbit interferometry package released, *EOS*, *Trans. Am. geophys. Un.,* **85**(5), 47.

Royden, L. H. & Papanikolaou, D. J., 2011. Slab segmentation and late Cenozoic disruption of the Hellenic arc, *Geochem. Geophys. Geosyst.,* **12,** doi:10.1029/2010GC003280.

Sachpazi, M. *et al.*, 2007. Moho tomography under central Greece and its compensation by Pn time-terms for the accurate location of hypocenters: the example of the gulf of Corinth 1995 Aigion earthquake, *Tecnophysics,* **440,** 53–65.

Seismicity Catalog. Available at: www.gein.noa.gr.

Serpetsidaki, A., Sokos, E. & Tselentis, G.-A., 2010. Study of the 2nd December 2002 Vartholomio earthquake (Western Peloponnese) M5.5 aftershock sequence, *Bull. geol. Soc. Gr.,* **XLIII** (4), 2174–2182.

Sodoudi, F. *et al.*, 2006. Lithospheric structure of the Aegean obtained from P and S receiver functions, *J. geophys. Res.,* **111,** B12307, doi:10.1029/2005JB003932.

Sokos, E. & Zahradnik, J., 2007. ISOLA-A Fortran code and a Matlab GUI to perform multiple-point source inversion of seismic data, *Comput. Geosci.,* **34,** 967–977.

Sokos, E.N. *et al.*, 2012. The January 2010 Efpalio earthquake sequence in the western Corinth Gulf (Greece), *Tectonophysics,* **530–531,** 299–309.

Stiros, S., Moschas, F., Feng, L. & Newman, A., 2013. Long-term versus short-term deformation of the meizoseismal area of the 2008 Achaia–Elia (M_W 6.4) earthquake in NW Peloponnese, Greece: evidence from historical triangulation and morphotectonic data, *Tectonophysics,* **592,** 150–158.

Tarantola, A. & Valette, B., 1982. Generalized nonlinear inverse problem solved using the least squares criterion, *Rev. Geophys. Space Phys.,* **20,** 219–232.

Tselentis, G.-A., Melis, N.S., Sokos, E. & Papatsimpa, K., 1996. The Egion June 15, 1995 (6.2 ML) earthquake, Western Greece, *Pure appl. Geophys.,* **147,** 83–98.

Vernant, P., Reilinger, R. & McClusky, S., 2014. Geodetic evidence for low coupling on the Hellenic subduction plate interface, *Earth planet. Sci. Lett.,* **385**(C), 122–129.

Waldhauser, F., 2001. HypoDD: A computer program to compute double-difference hypocenter locations, Open-File Rep., U.S. Geol. Surv., 01-113.

Waldhauser, F. & Ellsworth, W.L., 2000. A double-difference earthquake location algorithm: method and application to the Northern Hayward fault, California, *Bull. seismol. Soc. Am.,* **90,** 1353–1368.

Wiemer, S. & Zuniga, R.F., 1994. ZMAP, a software package to analyze seismicity, *EOS, Transactions, Fall Meeting,* AGU, **75,** 456, San Francisco, CA, USA.

Zahradník, J., Serpetsidaki, A., Sokos, E. & Tselentis, A., 2005. Iterative deconvolution of regional waveforms and a double–event interpretation of the 2003 Lefkada earthquake, Greece, *Bull. seism. Soc. Am.,* **95,** 159–172.